Check for updates

Novel dual-functional manganese stannate thin film for acetone gas sensing and photocatalytic methyl orange degradation

Sharanu,[ad] Akshayakumar Kompa,[b] Dhananjaya Kekuda, [a] M. S. Murari[c] and Mohan Rao K [*a]

Increasing health concerns due to pollution has led to the development of various materials to control exposure to pollutants such as toxic gases and contaminated water. In this study, novel manganese stannate (MTO) composite thin films were synthesized *via* sol–gel spin coating and their structural, morphological, and chemical properties were extensively characterized. In addition, their photocatalytic and gas-sensing abilities were evaluated. In photocatalysis, degradation efficiency measures of how well a photocatalyst can degrade pollutants or dyes under light exposure. Remarkably, the MTO film exhibited a high degradation efficiency of 67% for methyl orange (MO) dye when exposed to UV light for 150 minutes. We also examined the gas-sensing properties of the MTO thin films, particularly their response to acetone. In gas sensors, sensitivity is often reported as a percentage, indicating the relative change in the sensor's response per unit change in analyte concentration. Herein, the sensors displayed a linear response within the 1–9 ppm range of acetone concentration at an operating temperature of 200 °C. They also exhibited excellent selectivity, sensitivity, and repeatability, thus emerging as promising candidates for acetone gas-sensing applications. A sensitivity of 22% was achieved by the sensors, allowing for a low detection limit of 1 ppm, which indicated their high sensitivity towards acetone gas. Moreover, the MTO sensor exhibited response and recovery times of 15 and 16 seconds, respectively. Based on these results, the MTO thin film is a potential material for photocatalytic MO degradation and a gas sensor for acetone detection.

1. Introduction

The increasing demand for multi-functional devices has led to the exploration of functional materials that can serve multiple applications, offering versatility and efficiency. One example is metal stannate thin films, which possess at least two or more functionalities.[1] Recently, metal stannate thin films have garnered significant attention from researchers owing to their intriguing properties.[2–7] The morphologies of metal stannate thin films play a crucial role in determining the performance of sensors and enhancing the photocatalytic activities of these materials.[8,9] Metal stannate thin films such as Mn_2SnO_4 (MTO) exhibit a wide range of unique properties, such as superconductivity, ferromagnetism, and ferroelectricity.[5] Metal stannate

thin films can be used as electrical, photocatalytic, and magnetic sensors, showcasing their multi-functionality.[10,11] Furthermore, its desirable structural, morphological, electrical, optical, and thermal properties make MTO a particularly appealing metal stannate for various applications in electronics and energy technologies.[12,13] Manganese shows multiple oxidation states, leading to a broad spectrum of performance capabilities.

Furthermore, manganese tin oxides exhibit diverse phases that contribute to their many physical properties, which enhance our understanding of these materials. Researchers continue to study the properties of Mn_2SnO_4 (MTO) to unlock its full potential. MTO has already demonstrated usefulness in applications such as Li-ion batteries,[9] photocatalysis,[10] and spintronics.[14]

Recently, there has been growing interest in precisely detecting volatile organic compounds (VOCs) considering the concerns related to industrial safety, human health management, and environmental protection.[15] Acetone gas (C_3H_6O) is extensively used in industrial settings, pharmaceuticals, and laboratory facilities. It poses flammability and explosion risks, and prolonged exposure to the gas can harm various organs of the body.[16] Consequently, the fabrication of acetone-sensing

aDepartment of Physics, Manipal Institute of Technology, Manipal Academy of Higher Education, Manipal, 576 104, India. E-mail: kmohan.rao@manipal.edu

bEngineering Product Development, Singapore University of Technology and Design, Singapore

cNITTE (Deemed to be University), Nanoscience Research Laboratory, Department of Physics, NMAM Institute of Technology, NITTE, Karkala, Karnataka, 574110, India

dDepartment of Engineering Science and Humanities, Thakur College of Engineering and Technology, Mumbai 400101, India

detectors has garnered increased attention for health monitoring. Additionally, accurate acetone sensing is crucial for non-invasive diabetes diagnosis, wherein the concentration of acetone in a person's breath is a significant indicator for assessing diabetes in patients. In healthy individuals, the acetone concentration in the respiratory system is typically below 1 ppm (ranging from 0.3 to 0.9 ppm) but can exceed 1.8 ppm in diabetic patients.[16–18] Therefore, detecting acetone gas concentrations under parts per million (ppm) concentration is crucial for diabetes diagnosis and monitoring. Gas sensors, particularly those using metal oxide semiconductors such as MTO, offer a cost-effective and straightforward method for detecting hazardous gases compared with conventional systems. The crystalline and porous nature of MTO promotes the adsorption of atmospheric oxygen, enhancing its sensitivity as a gas sensor for acetone detection.

Numerous countries worldwide are grappling with severe water scarcity and ecological challenges stemming from the extensive contamination of water sources by various organic dyes.[8] Industries such as printing, textiles, painting, food, cosmetics, and pharmaceuticals release waste laden with harmful pollutants, giving rise to significant environmental concerns with far-reaching implications for ecosystems.[19–22] Methyl orange (MO) is a commonly used dye in the textile and chemical industries, but its presence in wastewater can pose a substantial health risk to living organisms. Researchers have explored various methods for degrading MO to address this issue, and metal oxide thin films have shown promise as potential catalysts in this process.

The Mn/Sn molar ratio is a crucial parameter for controlling the composition and properties of manganese tin oxide materials and directly impacts the porous structure of MTO thin films. Researchers often fine-tune this ratio to tailor the properties and porosity of MTO films for specific applications, such as gas sensors, photocatalysis, or energy-storage devices.[23–25] In the present study, an MTO thin film was developed by tuning the concentration of cations. We found that the Mn/Sn molar ratio significantly influences the materials' structural, morphological, and electrical properties. We then evaluated the MTO thin films' photocatalytic and gas-sensing capabilities.

2. Methodology

2.1. Fabrication of MTO thin films

The MTO thin film solution was prepared using stannous chloride pentahydrate (SnCl$_4$·5H$_2$O, 98%) and manganese acetate dihydrate (Mn(CH$_3$CO$_2$)$_2$·2H$_2$O, 98%) as the sources of tin and manganese cations. These cation sources were dissolved in 2-methoxy ethanol (solvent). Next, with 0.4 M selected as the total concentration (Mn + Sn), the Mn and Sn ratio was tuned as Mn/Sn = 1.5, 2, 2.5, and 3. After aging, the solution was left to stand for 24 h followed by coating on glass using a spin-coating system (Holmarc Model: HO-TH-5) at 2000 rpm for 30 s.[26–28] The coated substrates were preheated at 250 °C for 6 min to eliminate the solvents and any other organic residuals. The coating was repeated until a thickness of 300 nm was attained. Finally, the MTO films were annealed at 500 °C to obtain a crystalline

ternary material. To identify the samples, the films were coded as Mn/Sn (1.5), Mn/Sn (2), Mn/Sn (2.5), and Mn/Sn (3), respectively.

2.2. Characterization of the MTO thin films

The post-annealed films underwent extensive characterization to examine their properties. The structural parameters were assessed using an X-ray diffraction instrument (XRD; Empyrean Malvern Panalytical) equipped with a Cu-Kα source for X-ray generation. The morphology of the films was observed by field emission scanning electron microscopy (FESEM; Carl Zeiss Sigma), atomic force microscopy (AFM; Park System), and transmission electron microscopy (TEM; Titan Themis 300 kV from FEI, Thermo). The chemical composition of the films was analyzed using an X-ray photoelectron spectroscopy instrument (XPS; Shimadzu Axis Supra) equipped with an Al-Kα source for X-ray generation. In addition, a Holmarc contact angle meter (Model No. HO-ED-M-01) was used for the wettability studies and a Keithley 3706 source meter for the electrical studies.

2.3. Gas-sensing setup

Acetone gas was used to analyse the gas-sensing activity of the MTO samples. The gas sensing chamber had a capacity of 3.05 × 10^4 cm^3. The electrodes were fabricated using silver conducting paste. The gas concentrations of the target gas (from an acetone cylinder procured from Chemix with a purity of 99.0%) and synthetic air (80% nitrogen and 20% oxygen) were controlled using mass flow controllers (MFCs), with a total gas flow of 500 sccm. Sensor resistance was initially stabilised by purging the chamber with synthetic air. The sensor's response was tested at different temperatures to determine the optimal operating temperature. The target gas (acetone) diluted with synthetic air was introduced into the chamber, and the sensor's resistance change in the presence of dry air and acetone was continuously recorded. Acetone gas concentration was adjusted from 1 ppm to 9 ppm in 2 ppm increments. The sensitivity is given by the equation $s = \dfrac{R_a - R_g}{R_a} \times 100$, where R_a is dry air resistance and R_g is acetone gas resistance. The response and recovery times were measured as the time taken for the resistance to change by 90% in acetone gas and air, respectively.

2.4. Photocatalytic setup

The degradation of the MO dye solution was conducted to assess the photocatalytic activity of the MTO samples. For this study, the MTO films were immersed in MO solution in the dark followed by light illumination using a UV lamp (11 W). This test was carried out in a closed chamber for 150 min. At regular intervals, aliquots were collected to test the degradation level using a spectrophotometer.

3. Results and discussion

3.1 Structural analysis

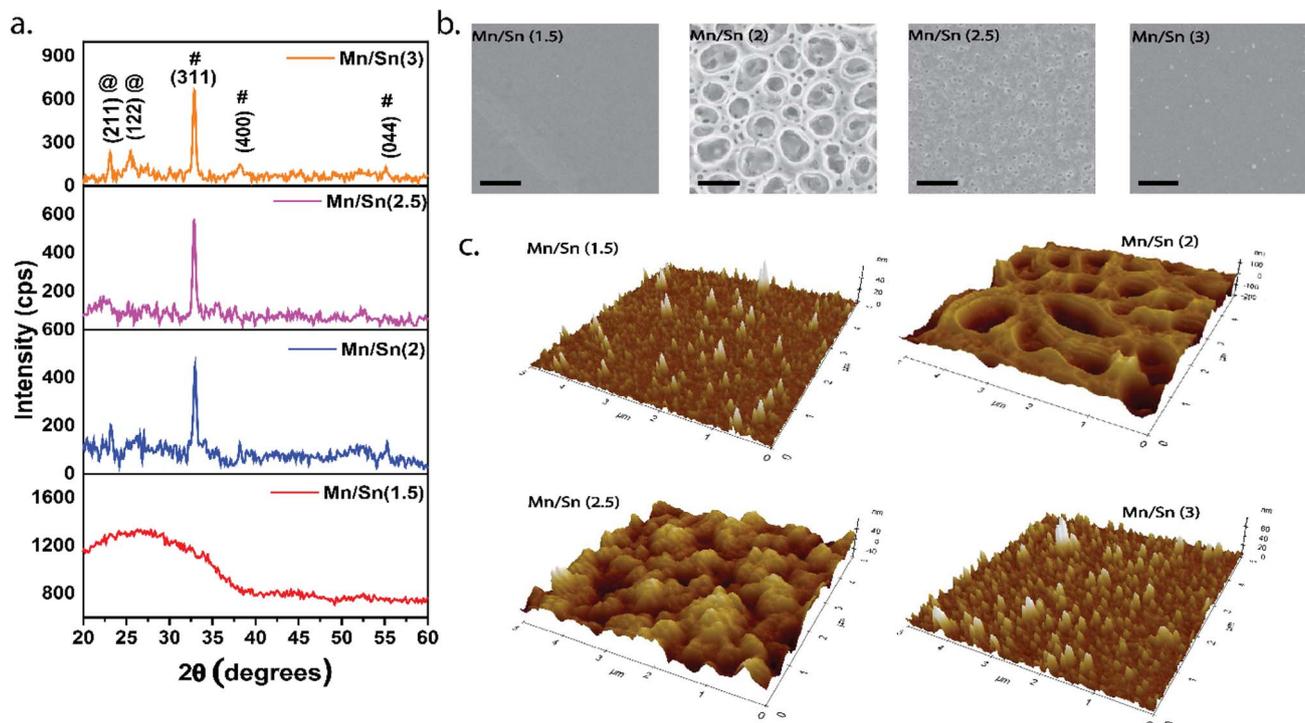The XRD patterns of the MTO thin films made with varied Mn/Sn molar ratios are shown in Fig. 1a. The Mn/Sn molar ratio

Fig. 1 (a) XRD patterns of MTO thin films fabricated with varying Mn/Sn ratios, where the identified peaks correspond to the @-Mn_2O_3 phase and #-Mn_2SnO_4 phase, (b) morphology (FESEM) of the samples with unique nano-level features (scale bar is 1 μm) and (c) topography (AFM) of the samples showing roughness variation due to a change in the cation ratio.

influences the growth of the MTO film and is an important parameter that influences the stoichiometry of the thin films. The ideal stoichiometry value is essential for obtaining pure and highly crystalline Mn_2SnO_4 phase-containing thin films. The film prepared with a Mn/Sn molar ratio of 1.5 showed an amorphous nature. This might be due to a deficit of Mn in the film, which would not meet the optimal stoichiometry value of Mn_2SnO_4. The Mn_2SnO_4 structure was observed for the samples prepared with Mn/Sn molar ratios of 2, 2.5, and 3. The optimization continued until the Mn/Sn molar ratio reached 3; whereby an excess of Mn was the origin of the Mn_2O_3 phase as a by-product. The intensity of the peak related to the Mn_2O_3 phase increased as Mn/Sn molar ratio was increased.

The growth of the film toward the (311) plane corresponded to the Mn_2SnO_4 inverse spinel cubic phase. The films contained a by-product phase, which could be observed by the (211) and (122) planes, corresponding to Mn_2O_3. The JCPDS card numbers (74-2378) and (41-1442) confirmed phase confirmation. The obtained Mn_2SnO_4 and Mn_2O_3 phases agreed with the reported works.[9,29]

The crystalline size of the nanomaterials was calculated using Scherrer's formula, which considers the broadening (FWHM) of diffraction peaks due to size effects and intrinsic strain. Since diffraction peak broadening arises from both physical and instrumental contributions, it must be corrected using the below equation:

$$\beta_{hkl} = [(\beta_{hkl}{}^2)_{\text{measured}} - (\beta_{hkl}{}^2)_{\text{instrumental}}]^{1/2}. \tag{1}$$

The actual broadening related to the material was estimated using the above relation. Further, this value was used in Scherrer's equation to evaluate the crystallite size of our material. This procedure has been well-reported by several researchers to compute the crystallite size of nanomaterials (nanoparticles/thin films).[26,30,31]

The average crystallite size was determined using Scherrer's equation. The relations are given below:[27]

$$D = \frac{k\lambda}{\beta \cos \theta} \tag{2}$$

$$\varepsilon = \frac{\beta}{4 \tan \theta}, \tag{3}$$

where k, β, λ, ε, θ, and D indicate the shape factor, FWHM, wavelength of X-ray radiation, strain, Bragg angle, and average crystallite size, respectively.

The average crystallite size determined using the half-width maxima of the (311) plane ranged from 21 to 23 nm. According to Table 1, samples prepared with a Mn/Sn molar ratio of 3 exhibited larger average crystallite sizes than the other Mn/Sn

Table 1 Structural parameters computed from XRD data

Sample code	Mn/Sn (2)	Mn/Sn (2.5)	Mn/Sn (3)
Crystallite size D (nm)	21.6	22.2	23.3
Micro strain ε (10^{-3})	1.6	1.5	1.4

molar ratio samples. This might be because the Mn_2O_3 phase was agglomerated with Mn_2SnO_4, enhancing its average crystallinity. The strain was less for the Mn/Sn samples with a molar ratio of 3, which might be attributed to their fewer film defects. Smaller average crystallite sizes typically result in a larger surface area per unit volume of the material. This increased surface area provides more active sites for photocatalytic reactions and gas molecules to interact with the material. As a result, the Mn/Sn = 2 samples with smaller average crystallites may be more sensitive to photocatalytic activity and gas adsorption due to the larger available surface area.

3.2 Morphology of the MTO surface

We studied the surface morphology of the MTO samples with various Mn/Sn molar ratios. FESEM microphotographs of the MTO samples are shown in Fig. 1b. The micrographs showed that the Mn/Sn molar ratio significantly impacted the surface characteristics of the deposited films. The materials were evenly spread throughout the substrate. The micrographs further show that the films were homogenous and crack-free for all the samples. The films prepared with Mn/Sn molar ratios of 1.5 and 3 displayed small spherical grains distributed over the planar surface. The samples prepared at Mn/Sn molar rations of 2 and 2.5 show the presence of a porous structure on the surfaces, as shown by the fine unique discontinuous networks.[32,33] The surface of the Mn/Sn = 2 sample exhibited a dense arrangement of pores, with each pore having a diameter of roughly 0.7 μm. The different Mn/Sn molar ratios resulted in variations in the composition of the MnO–MTO material. Manganese oxide (Mn_2O_3) had a distinct crystal structure and properties compared with Mn_2SnO_4. When the molar ratio was adjusted, the relative proportions of these oxides in the final MnO–MTO material changed, thereby affecting its morphological structure and properties.

3.3 Topography of the MTO surface

Fig. 1c depicts the three-dimensional topography of the MTO films recorded using AFM, showing a random distribution of grains of different sizes across the substrate for the Mn/Sn = 1.5 sample. Meanwhile, the surfaces of Mn/Sn samples with molar ratios of 2–3 showed a lower number of grains and an increment in grain size. The film's roughness ranged from 4 to 50 nm, consistent with previously published work.[34] The surface roughness of the MTO film, obtained with an Mn/Sn (2) ratio of 50 nm, makes it well-suited for surface-related applications, such as photocatalysis and gas sensors. In these applications, the adsorption of molecules on the surface plays a crucial role in initiating reactions. Films with a high surface roughness can adsorb a greater number of species, leading to significant alterations in their properties and enabling superior performance in specific applications.

3.4 TEM analysis

It was essential to obtain intricate information about the materials' structure, morphology, and elemental composition. Fig. 2 shows the TEM image of the MTO thin film (Mn/Sn = 2 sample). Fig. 2a shows that the Mn_2SnO_4/Mn_2O_3 composite featured numerous three-dimensional spherical structures that were densely packed together and exhibited a uniform size distribution. Fig. 2b depicts the composite material's selected area electron diffraction (SAED) pattern, which exhibits multiple concentric rings. These rings could be attributed to specific crystal planes, including the (122) and (044) planes of Mn_2O_3, as well as the (311) and (040) planes of Mn_2SnO_4. This observation suggests the presence of two distinct phases within the material: Mn_2SnO_4 and Mn_2O_3. Fig. 2c depicts the high-resolution transmission electron microscopy (HRTEM) images of MTO, revealing lattice spacing values of 0.27, 0.26, 0.22, and 0.16 nm. These values correspond to the (122), (311), (220), (040), and (044) crystallographic planes of the materials' Mn_2O_3 body-centred cubic phase and Mn_2SnO_4 inverse spinel cubic phase. The TEM spectra in Fig. 2d confirmed the presence of Mn, Sn, and O elements in the thin films.

3.5 Chemical composition of the MTO film

Fig. 3 shows the XPS spectra of the Mn/Sn (2) Mn/Sn (2.5) thin films annealed at 500 °C. The survey scan spectrum in Fig. 3a shows the presence of Mn, Sn, O, and C elements. The deconvoluted narrow scans for the Mn/Sn (2) and Mn/Sn (2.5) thin films related to O 1s, Mn 2p, and Sn 3d are presented in Fig. 3b and c. The deconvoluted spectrum of O-1s revealed the presence of multiple sub-peaks labelled as O-I (531.3 eV) and O-II (529.81 eV), corresponding to adsorbed oxygen and O^{2-}. The obtained results agreed well with previously published work.[35] The presence of oxygen vacancies in MTO suggested the formation of non-stoichiometric Mn_2SnO_4, which can be expressed as $Mn_2SnO_{4-\delta}$. These oxygen vacancies, acting as intrinsic crystal defects, are crucial for modulating the electronic structure and charge-carrier concentration. While such defects are not distinctly visible in the XRD pattern, their presence was evident from the XPS peak ratios. Regarding the contribution of different types of oxygen species, our analysis suggests that chemisorbed oxygen (O^-, O_2^{2-}, O_2^-) played a dominant role in gas sensing rather than lattice oxygen (O^{2-}) or surface oxygen. The adsorbed oxygen species capture electrons from the conduction band, creating a depletion layer and increasing resistance. Upon exposure to acetone, these species participate in redox reactions, releasing electrons back into the material and reducing resistance, which enhances the sensor response. The increased oxygen vacancies in the Mn/Sn (2) films facilitated the adsorption of chemisorbed oxygen species, thereby improving sensitivity, selectivity, and response speed. In Mn_2SnO_4, manganese is often in the Mn^{2+} oxidation state. Mn $2p_{3/2}$ at ∼641 eV and Mn $2p_{1/2}$ at ∼652 eV confirms the Mn^{2+}. Mn $2p_{3/2}$ at ∼643–645 eV and Mn $2p_{1/2}$ at ∼654–656 eV confirms the Mn^{3+}. The existence of Mn^{3+} confirms the Mn_2O_3 phase in the films, which correlated well with the XRD and TEM results. Mn oxidation states play a vital role in gas sensing by influencing the adsorption and desorption processes. Mn exists in multiple valence states (Mn^{2+} and Mn^{3+}), and the redox transitions between these states facilitate electron exchange during gas interactions. Moreover, the Mn^{2+}/Mn^{3+} ratio affects the
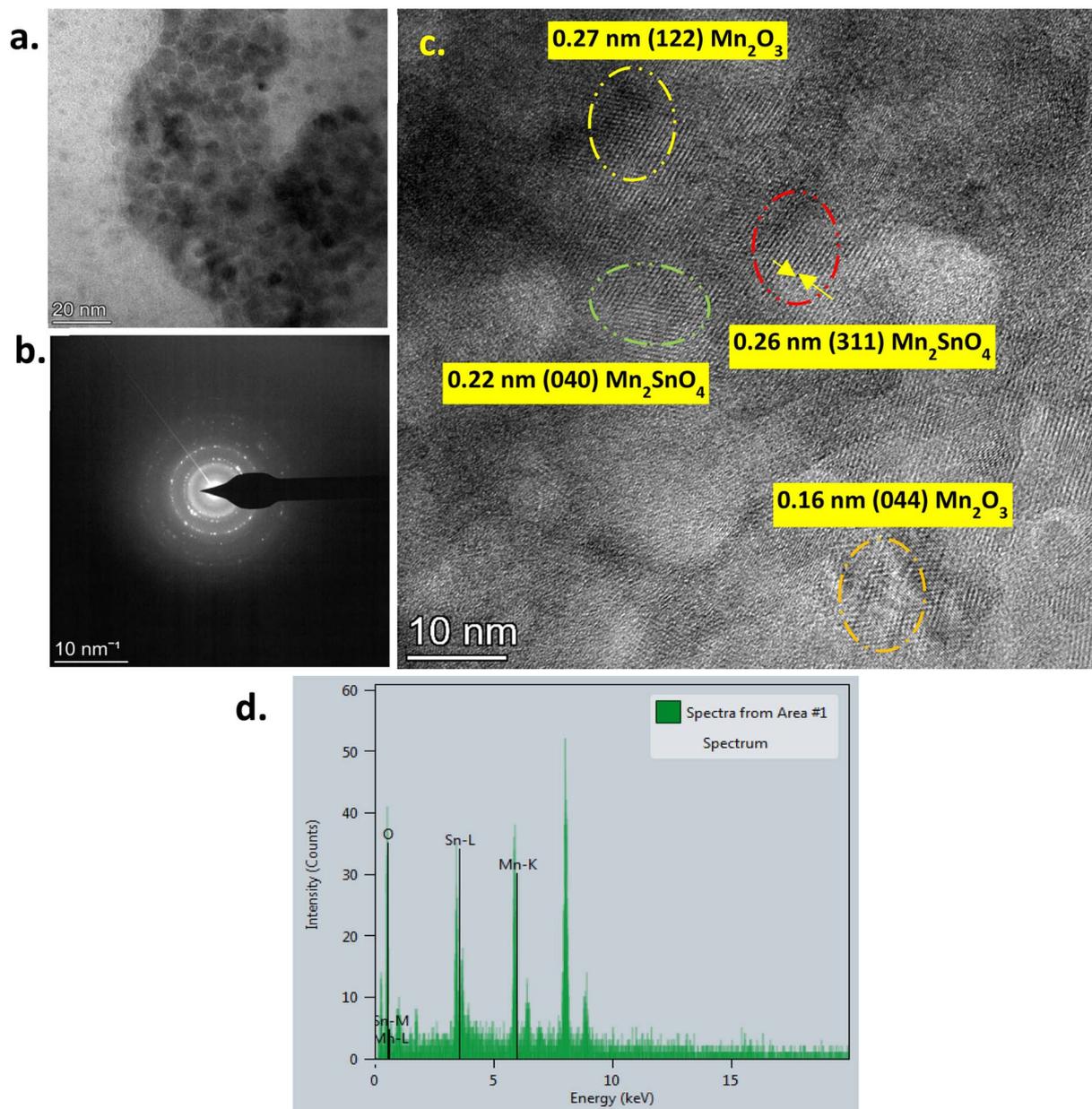
Fig. 2 (a) TEM images of the sample with a Mn/Sn molar ratio of 2. (b) Selected area electron diffraction (SAED) pattern indicating the presence of crystalline phases. (c) HRTEM image showing the mixed phases of Mn_2SnO_4 and Mn_2O_3. (d) Elemental composition.

density of oxygen vacancies, which in turn enhances the gas-sensing response. XPS peak areas attributed to oxygen vacancies increased from 39% for pure Mn_2SnO_4 to 59% for the Mn/Sn (2) MTO thin films, indicating that a higher Mn content promoted oxygen vacancy formation, thereby improving sensing performance. The narrow scan for Sn-3d revealed peaks corresponding to Sn3-$d_{3/2}$ and Sn3-$d_{5/2}$ and confirmed the presence of Sn^{4+} in the sample. The binding energy difference between Sn-3$d_{3/2}$ and Sn-3$d_{5/2}$ was 8.37 eV, which was consistent with published data.[8] Table 2 provides the peak positions, full width at half maximum (FWHM), and elemental quantifications for Mn-2p, Sn-3d, and O-1s, indicating that changing the Mn/Sn ratio from 2 to 2.5 slightly increased the amount of Mn. The binding energies and FWHM values implied that both Mn and

Sn were present in specific oxidation states (Sn^{4+}, Mn^{2+} and Mn^{3+}), while the oxygen was bonded in oxide forms, contributing to the structure of the Mn/Sn oxide thin films.[36,37]

3.6 Electrical properties

Table 3 summarizes the MTO thin films' electrical parameters: resistivity, carrier concentration, and mobility. These parameters were calculated using a software interface integrated with the Keithley 3706 source meter, which automates the process. The formulae applied in the software are as follows:

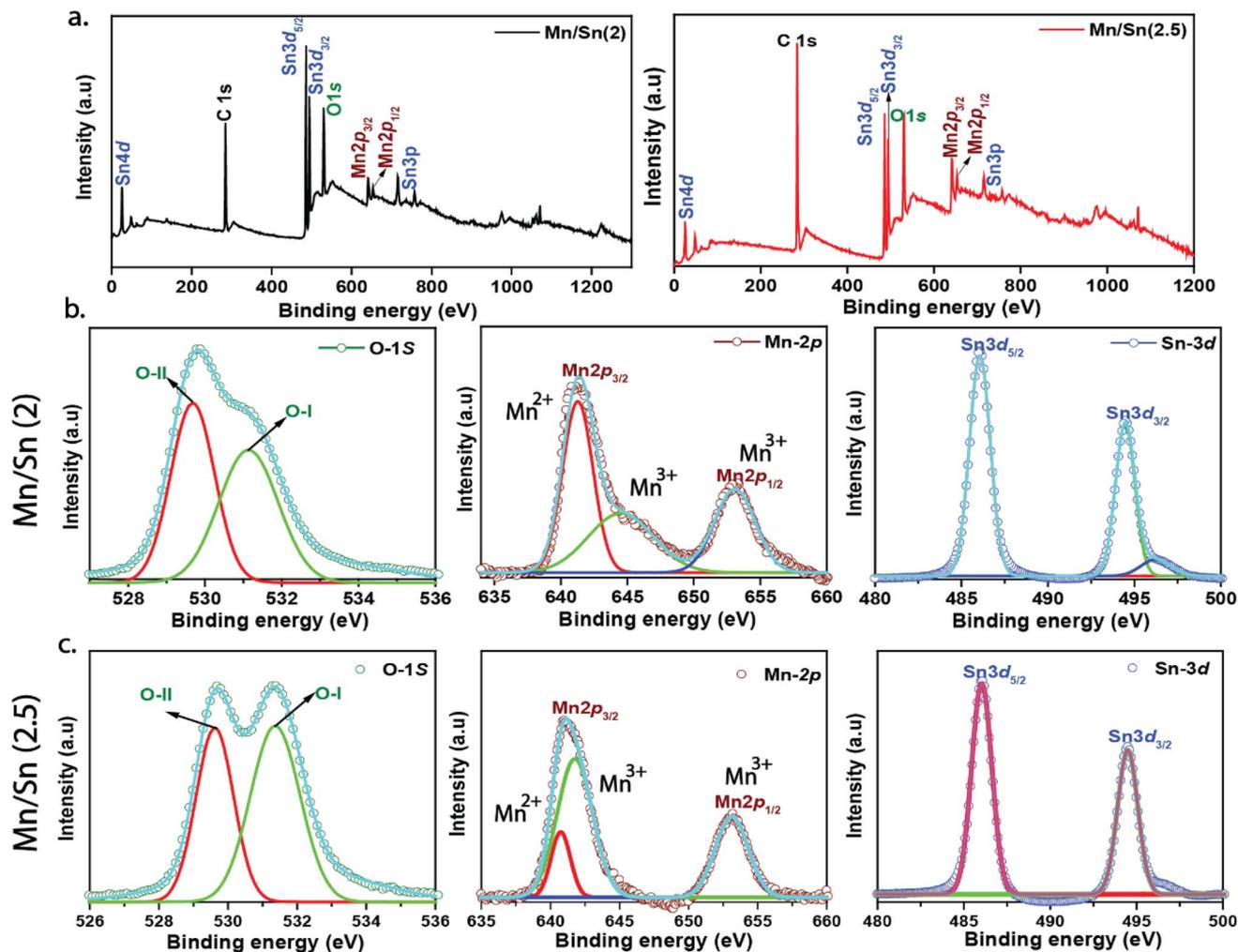Resistivity:

$$\rho = R_s t \qquad (4)$$

Fig. 3 (a) Survey scan to identify all the essential elements in the Mn/Sn = 2 and 2.5 materials; (b) and (c) deconvoluted narrow scans of Mn/Sn (2) and Mn/Sn (2.5) thin films for O 1s, Mn 2p, and Sn 3d.

Table 2 Peak position and elemental composition of Mn, Sn, and O for the thin films with Mn/Sn ratios of 2 and 2.5

Elements	Binding energy (eV)	FWHM (eV)	Atomic (%) Mn/Sn (2)	Mn/Sn (2.5)
Sn-3d$_{5/2}$	486.0 ± 0.01	1.4 ± 0.02	2.2	2.7
Sn-3d$_{3/2}$	494.4 ± 0.01	1.3 ± 0.02		
Mn-2p$_{3/2}$	641.0 ± 0.01	1.0 ± 0.01		
Mn-2p$_{1/2}$	652.0 ± 0.01	1.0 ± 0.01		
O-1s	531.3 ± 0.02	1.8 ± 0.05		

Carrier concentration:

$$n = \frac{1}{R_{\mathrm{H}}q} \tag{5}$$

Mobility:

$$\mu = \frac{1}{\rho n e}. \tag{6}$$

The resistivity values ranged from 0.3 to 12 Ω cm for the different Mn/Sn molar ratio samples. The Mn/Sn (1.5) sample

Table 3 Electrical parameters of MTO thin films

Samples	Resistivity (ohm cm^{-1})	Carrier concentration (cm^{-3})	Mobility (cm^2 V^{-1} s^{-1})
Mn/Sn (1.5)	12	8×10^{14}	14
Mn/Sn (2)	0.3	2×10^{15}	8
Mn/Sn (2.5)	0.5	5×10^{14}	12
Mn/Sn (3)	0.5	1×10^{15}	10

had the highest resistivity of 12 Ω cm, indicating it is the least conductive. This high resistivity might be due to a lower carrier concentration or more defect states that trap carriers, thereby reducing the mobility. The Mn/Sn (2) sample exhibited a low resistivity, possibly due to the fewer carrier entrapment states. The mobility values ranged from 8 to 12 cm^2 V^{-1} s^{-1} for the different Mn/Sn molar ratio samples. The Mn/Sn (2) sample had the lowest mobility of 8 cm^2 V^{-1} s^{-1}, which might indicate higher scattering rates or more defects. The carrier concentration ranged from 8×10^{14} to 2×10^{15} cm^{-3}. The Mn/Sn (2) sample had the highest carrier concentration of 2×10^{15} cm^{-3}, which aligned with its low resistivity, suggesting a high density of free charge carriers that contribute to electrical conduction. Higher Mn/Sn ratios decreased the resistivity due to the increased carrier concentration, though the mobility might be reduced due to the greater number of scattering events or defects. These changes align with the expected behavior of doped semiconductors, wherein the doping level influences the electrical conductivity. These electrical properties were influenced by defects such as oxygen vacancies and Mn/Sn interstitials, consistent with prior studies.[38]

3.7 Wettability study

Surface wettability, determined by the surface structure and chemical composition, is a crucial property with applications in self-cleaning and antifogging coatings.[39,40] Hydrophilic or superhydrophilic surfaces are particularly desirable for expanding the utility of metal oxides in biosensors or chemical sensors.[41] Surface wettability is a crucial aspect of photocatalysis, reflecting the physical interaction between a liquid and a material's surface. In photocatalytic applications, a hydrophilic surface is imperative as it facilitates the adsorption of water-soluble dye molecules onto the nanostructures on the material surface. Before considering a material for use as a photocatalyst, it is essential to assess its wettability to ensure its compatibility with water-based solutions. To confirm the hydrophilic nature of our material, we conducted wettability studies. This involved measuring the contact angle of a water droplet on the surface of the thin film. Contact angle measurements provide a valuable insight into a surface's hydrophilic properties; whereby a higher contact angle indicates a lower affinity towards water-based solutions, while a lower contact angle signifies a higher affinity. In the context of photocatalysis, a low contact angle is desirable as it allows for increased interaction between the dye molecules and the photocatalyst surface, thereby enhancing the efficiency of the photocatalytic process. In liquid formulations, the contact angles help assess how modifications to the liquid influence its spreading behavior.

Young's equation relates the contact angle (θ) of a droplet on a solid surface to the interfacial tensions between the liquid–vapor phase (Y_{lv}), solid–vapor (Y_{sv}), and solid–liquid (Y_{ls}) interfaces and is expressed by the equation below:[40]

$$Y_{sv} = Y_{ls} + Y_{lv}\cos\theta, \tag{7}$$

where liquid–vapor surface tension is denoted as $\cos\theta$. This relation can be rearranged as follows:

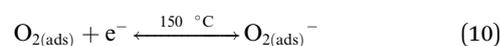$$\cos\theta = \frac{Y_{sv} - Y_{ls}}{Y_{lv}}. \tag{8}$$

At equilibrium, the contact angle reflects the balance of the following forces: adhesive forces between the liquid and solid (Y_{ls}) and the cohesive force within the liquid–vapor (Y_{lv}) or solid–vapor (Y_{sv}). Θ, being a contact angle, determines surface wettability, where a contact angle <90° indicates a hydrophilic surface with high water affinity, while a contact angle >90° indicates a hydrophobic surface with water resistance.
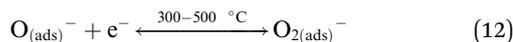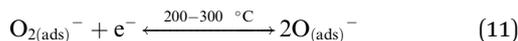
Fig. 6a illustrates the water droplet shapes on the MTO thin films with different Mn/Sn ratios. The contact angle measurements revealed low contact angles of 31° and 35° for both films (with Mn/Sn ratios of 2 and 2.5), indicating the hydrophilic nature of the films. The reason for their hydrophilicity can be correlated with the SEM images shown in Fig. 1c. The high porosity associated with the Mn/Sn = 2 molar ratio sample contributed to its lower contact angle than the Mn/Sn = 2.5 materials. From these observations, we can infer that the value of the contact angle is directly related to the microstructured characteristics of the film. Additionally, AFM results confirmed the high surface roughness of the sample, which also contributed to a reduction in the contact angle.

3.8 MTO as a gas sensor

Materials to be used for gas-sensing applications should possess characteristics desirable for the gas interaction with materials. The physical and chemical microstructures of the sensing material surfaces, whose interactions with gaseous mixtures result in the sensor responses, represent a crucial factor for fine-tuning the performance of gas sensors, particularly in terms of the sensitivity and selectivity. Nanostructures in a material can be dense or porous. When it comes to sensing materials made of dense surfaces, the gas can only be adsorbed on the surface since it cannot get inside the materials; however, when the material is porous, the gas can enter the nanostructures and interact with the inside nanostructures, thus improving the overall response of the material. In the current work, the appropriate Mn/Sn samples with molar ratios of 2 and 2.5 demonstrated porous natures, providing a high surface area for gas interaction. The detailed mechanism of sensing on the MTO surface is described below.

The typical sensing mechanism of metal oxide-based acetone gas sensors is as follows: when the sensor is exposed to air, oxygen molecules, which have a high electron affinity (0.43 eV), become adsorbed on the sensor's surface and extract electrons from the sensing layer. The specific oxygen ion species present on the surface of the gas sensor will vary depending on the operating temperature. This behaviour can be described using the following equations.[18,42]

$$O_{2(g)} \xleftrightarrow{\;80\,°C\;} O_{2(ads)} \tag{9}$$

$$O_{2(ads)} + e^- \xleftrightarrow{\;150\,°C\;} O_{2(ads)}{}^- \tag{10}$$

$$O_{2(ads)}^{-} + e^{-} \xleftrightarrow{200-300 \ ^\circ C} 2O_{(ads)}^{-} \qquad (11)$$

$$O_{(ads)}^{-} + e^{-} \xleftrightarrow{300-500 \ ^\circ C} O_{2(ads)}^{-} \qquad (12)$$

Operating temperature is one of the most essential parameters for gas sensors. As a result, the responses of the MTO sensor to 9 ppm acetone at various working temperatures were examined to determine the ideal working temperature. Gas species detected by the gas sensor rely on the sensing material and the sensor's operating temperature. Molecular ions generally tend to be stable at temperatures below 150 °C, whereas other ions become stable at higher temperatures. The sensor's sensitivity increases as the operating temperature rises owing to the decreased activation energy needed for gas adsorption and desorption. Nevertheless, there is an ideal operating temperature over which the film degrades, reducing the sensitivity of the sensing material.

Fig. 4a shows the responses of the MTO sensor to 9 ppm acetone gas at various operating temperatures. The sensor had a high sensitivity of 22% to 9 ppm acetone gas at a 200 °C operating temperature. The sensor's reaction to acetone gas diminished as the working temperature rose from 150 °C to 250 °C. When the temperature increased, the sensitivity of the sensor decreased considerably. A decrease in resistance at high operating temperatures is a widely observed phenomenon in resistive sensors, and it could be due to desorption playing a prominent role at higher operating temperatures. Fig. 4b shows a plot of the sensor response *versus* acetone gas
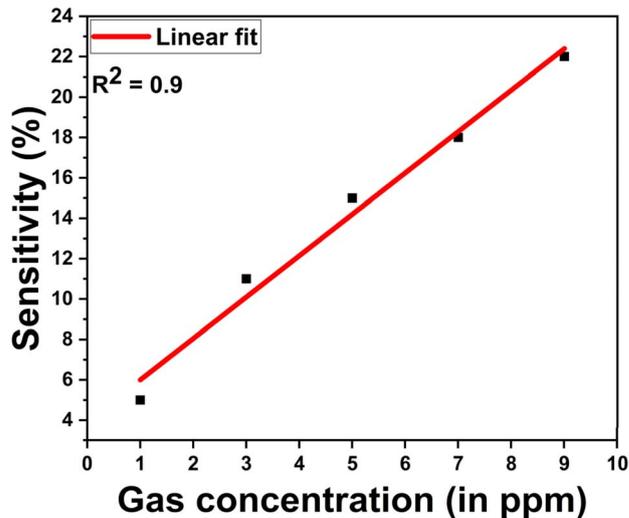

Fig. 5 Linear fitting plot of sensitivity *versus* gas concentration.

concentration and the dynamic response–recovery curves of the MTO sensor to acetone at 200 °C with concentrations ranging from 1 ppm to 9 ppm. From the plot, it can be seen that the responses of the MTO sensor increased with the acetone level in the given range. The rapidly growing responses suggest that the MTO sensor had a broad detection limit for acetone. With varying the concentration from 1 ppm to 9 ppm, the sensor gas sensitivity increased linearly, with the linear fitting plot shown in Fig. 5 supporting this.
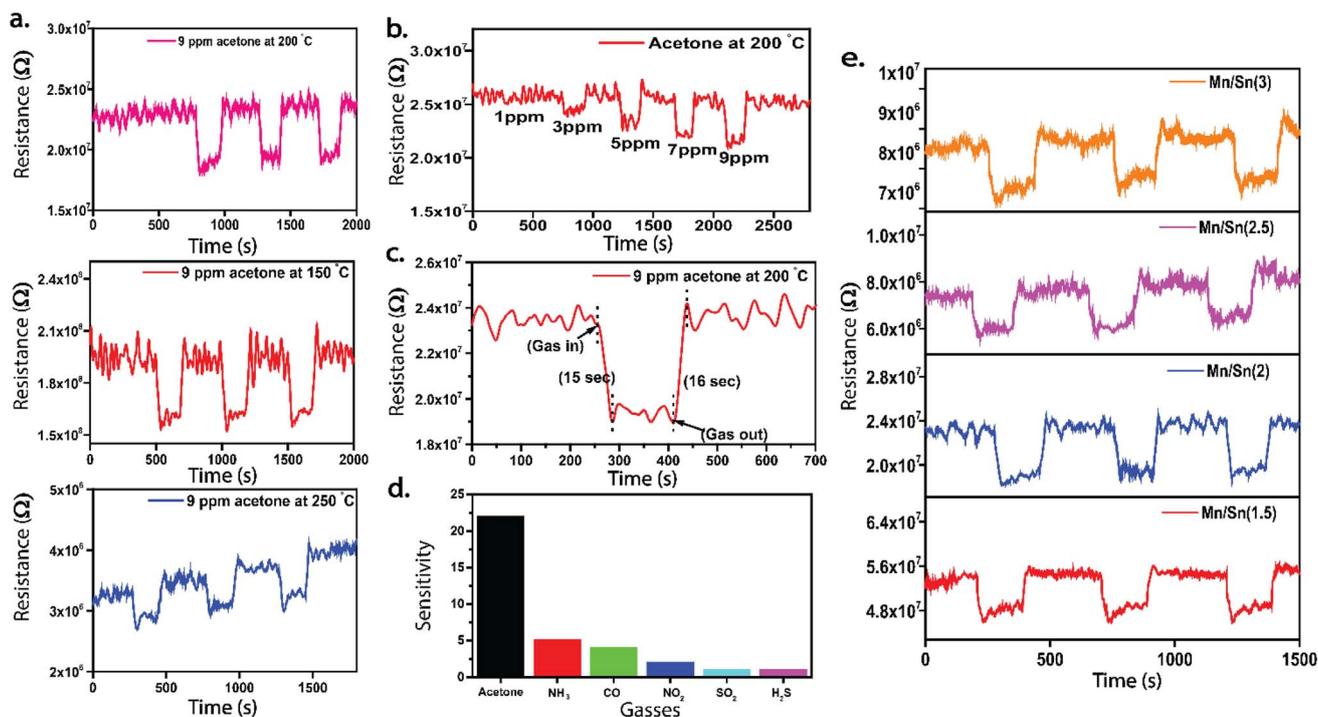

Fig. 4 (a) Acetone sensing at different operating temperatures using the Mn/Sn = 2 based sensors; (b) sensing of various concentrations of acetone at a 200 °C operating temperature; (c) response and recovery times for the MTO sensor for acetone sensing; (d) sensitivity of the MTO films for different gases; (e) repeatability of the sensing performance to check the stability of the film for long time usage.

The efficiency of gas sensors is significantly influenced by the reaction and recovery times. When exposed to acetone gas, the sensors underwent a redox reaction that increased the number of majority carriers, thereby decreasing film resistance. Film resistance gets saturated once all the chemisorbed oxygen has reacted with the reducing gas. Upon introducing synthetic air into the chamber, the resistance decreased. Fig. 4c shows film resistance recovery after discontinuing the reducing gas flow at 200 °C. The reaction time was the time taken by the sensor to reach 90% of its stable maximum resistance, while the recovery time was the time taken by the sensor to reach 10% of its original response. In this study, the average response and recovery times for the MTO films were calculated to be 15 seconds and 16 seconds, respectively, representing the best response. We compared the sensitivity and response/recovery time recorded in the current work with those of other oxide materials (Table 4); interestingly, MTO showed a good response to low ppm gas.

Apart from gas sensitivity, selectivity is another essential factor for gas sensors. Here, the MTO thin films were also used to sense various gases, like acetone, NH_3, CO, NO_2, SO_2, and H_2S, to understand the selective adsorption of gases on the films. Among the test gases, the films showed a significant response to acetone at a 200 °C operating temperature (Fig. 4d). The response of the MTO sensor to acetone was more than four times higher than its response to the other gases, indicating its good selectivity. At this temperature, acetone molecules adsorbed on the surface react with the already chemisorbed oxygen ions causing a release of trapped electrons back into the semiconductor's conduction band. Therefore, the electron depletion region diminishes, leading to a reduction in resistance. The potential chemical reactions between two gases on the nanostructured MTO surface can be described by the following formula.

$$CH_3COCH_{3(gas)} + 8O^- \rightarrow 3CO_2 + 8e^- + 3H_2O \quad (13)$$
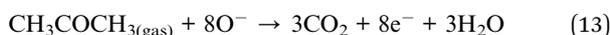
The repeatability and stability of the gas sensor for long term usage are also important for its practical use. As shown in Fig. 4e, the responses of the MTO sensor to 9 ppm acetone gas were measured in 3 consecutive tests at 200 °C. The results demonstrated that the sensor could maintains its initial response amplitude after 3 cycles. The response % (or sensor signal) and sensitivity are two different parameters. Here, Mn/Sn (1.5) exhibited a relatively higher response at a specific instance, but this did not necessarily imply it had the best overall gas-sensing performance. The key metric for

comparison is the change in resistance upon gas exposure, which was highest for Mn/Sn (2), leading to its better overall sensitivity, selectivity, and repeatability. The Mn/Sn (2) thin films also showed the highest stability and a consistent response/recovery behavior, making them the best candidate for practical sensing applications. Next, the stability of the films was analyzed based on multiple cycles of gas exposure to test for reproducibility. The findings indicated that the sensor had good reproducibility.

3.9 MTO as a photocatalyst

The photocatalytic performance of the MTO thin films was examined using methyl orange (MO) dye. MO shows a vivid orange color in water; it is carcinogenic, teratogenic, and toxic to aquatic organisms and other species. Prolonged exposure to this type of dye can lead to harmful effects on the organs of animals. Although degradation using particles has shown good performance, an extra step is needed to recover the particles from the reactor after the reaction. At the same time, catalysts in the form of a thin film do not require this additional step. Thus, we tested our novel MTO films for the degradation of MO. MO shows a prominent absorption at 465 nm. The change in the absorbance of MO over time reflects its degradation through photocatalytic treatment by MTO thin films under UV light irradiation. Initially, the absorbance at 465 nm will be high, indicating the presence of MO. As the reaction progresses, the absorbance at 465 nm should decrease, indicating MO degradation. The rate of this decrease can provide insights into the efficiency and kinetics of the degradation process.

Fig. 6b illustrates the degradation of MO under UV light in the presence of the MTO film as a catalyst. It could be seen that the degradation of MO increased with higher Mn/Sn molar ratios. Structural studies suggested that the amorphous nature of the Mn/Sn = 1.5 sample contributed to its lower MO degradation performance.

Fig. 6c displays the degradation efficiency (η) of the MO dye with all the samples. This was calculated using the following equation to quantify the effectiveness of the photocatalytic degradation process at each ratio:[45]

$$\eta = \frac{C_0 - C}{C_0} \times 100 \quad (14)$$

where C_0 is the initial concentration of MO, and C is the post degradation concentration.

The degradation efficiency of MO dye increased with the higher solution concentration and Mn/Sn molar ratio. The Mn/

Table 4 Comparison of the gas-sensing parameters with previous works for acetone gas sensing

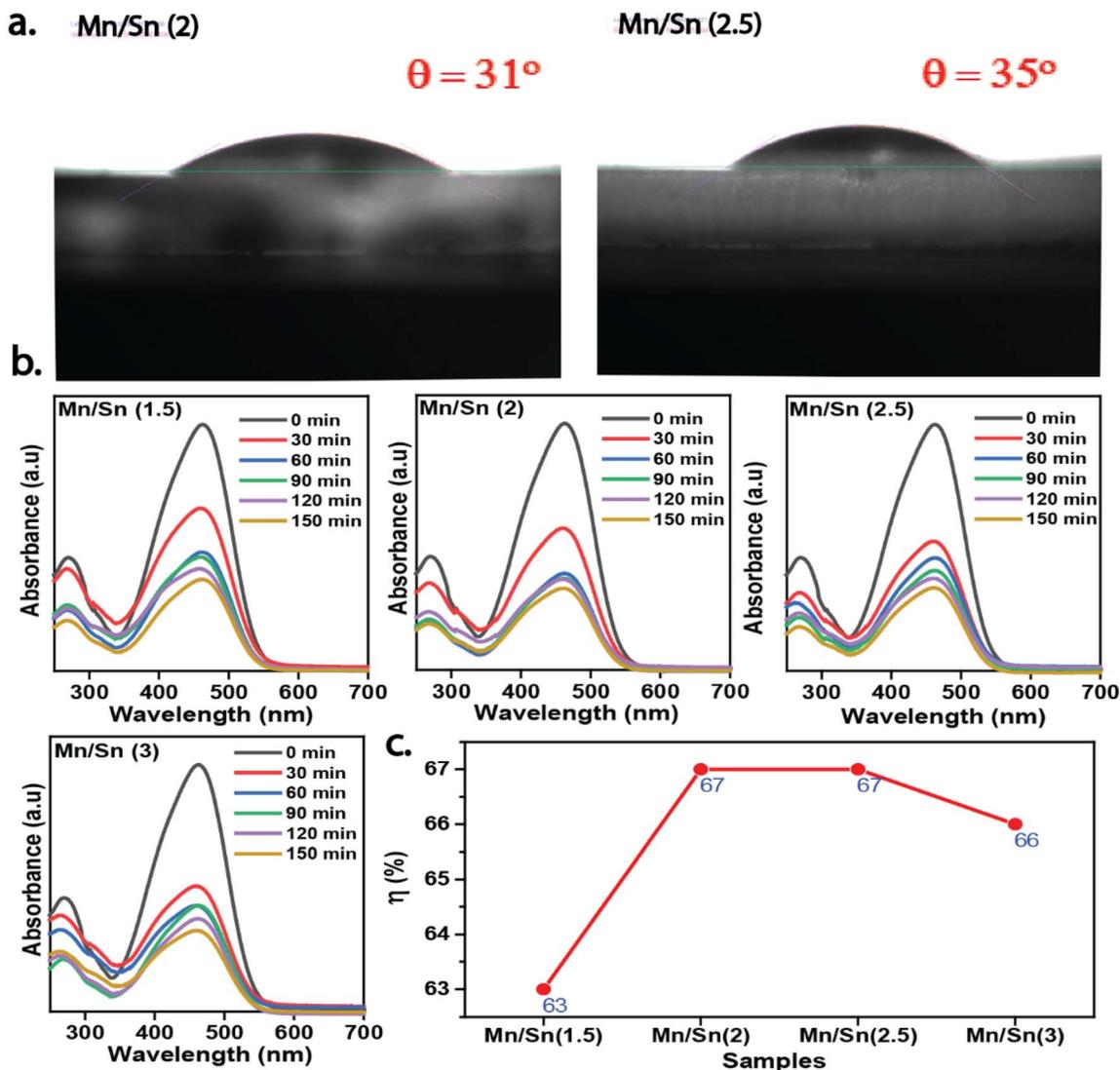| Material	Response (%)	Concentration (ppm)	Operating temperature (°C)	Selectivity	Reference
MTO (Mn/Sn = 2)	22	9	200	Moderate	Current study
Fe_2O_3/SnO_2	42.6	100	200	High	Wang et al., 2020 (ref. 43)
GO/ZnO	42.9	50	200	High	Zhang et al., 2022 (ref. 44)
$MnO_2/Gd_2O_3/SnO_2$	30	50	200	Low	Kumar et al., 2018 (ref. 16)

Fig. 6 (a) Contact angle measurements for the Mn/Sn = 2 and 2.5 thin films showing their highly hydrophilic natures; (b) photocatalytic degradation of MO using MTO as a thin film catalyst; (c) degradation efficiency of MTO films as a catalyst to degrade MO dye.

Table 5 Comparison of MO degradation efficiency with previous works

Material	Degradation efficiency (%)	UV exposure time (min)	Reference
MTO (Mn/Sn = 2)	67	150	Current study
Gd/Mn$_2$SnO$_4$	67	225	Muneer *et al.*, 2022 (ref. 10)
ZnO	55	360	Boughelout *et al.*, 2020 (ref. 46)
Cu$_2$O	53	360	Boughelout *et al.*, 2020 (ref. 46)

Sn = 2 and 2.5 molar ratio samples exhibited the highest degradation efficiencies, reaching up to 67% under 150 min of UV exposure. The current efficiency was also compared with other photocatalysts used for MO dye degradation (Table 5). It could be seen that other oxide materials typically took more than 150 min to degrade 50% of the dye. The MTO photocatalyst thus showed better degradation performance over other the reported materials in a shorter period.

4. Conclusions

Manganese tin oxide (MTO) composite thin films were successfully deposited using spin-coating technique with varying Mn/Sn molar ratios of 1.5, 2, 2.5, and 3, followed by annealing at 500 °C. All the films exhibited a polycrystalline nature, except those prepared with an Mn/Sn molar ratio of 1.5. The morphology of the films was analyzed using FESEM, AFM,

and TEM. Roughness values calculated for various Mn/Sn ratios ranged from 4 to 50 nm. FESEM images revealed that the morphological nanostructures comprised spherical grains and porous structures. TEM confirmed the presence of mixed phases of Mn_2O_3 and Mn_2SnO_4 in the films. The presence of Mn, Sn, and O elements with different oxidation states was confirmed through EDS and XPS. The gas-sensing mechanism of the MTO thin films towards acetone followed a surface-controlled chemisorption process based on redox reactions. At 200 °C, oxygen molecules from the ambient environment adsorbed onto the surface of the MTO film, forming O^-, O_2^-, or O_2^- species. When acetone (C_3H_6O) interacted with the surface, it underwent oxidation, releasing electrons back into the conduction band, thereby decreasing resistance. This electron exchange enhanced the sensor's response, resulting in a high selectivity, sensitivity (22%), and repeatability. The detection limit could be reduced to 1 ppm, making MTO a promising material for acetone gas sensing. The photocatalytic activity of the MTO thin films in the degradation of methyl orange (MO) dye was attributed to the generation of electron–hole pairs upon UV-light irradiation. The Mn_2O_3 and Mn_2SnO_4 phases in the film created heterojunctions that facilitated charge separation, reduced recombination, and enhanced photocatalytic efficiency. Photogenerated electrons reacted with dissolved O_2 to form superoxide radicals ($O_2^-\cdot$), while the holes oxidized water molecules to generate hydroxyl radicals ($^\cdot OH$). These reactive species break down MO into smaller, environmentally benign molecules. Samples with an Mn/Sn molar ratio of 2 exhibited the highest degradation efficiency (67%) in less than 150 minutes owing to the optimized charge-carrier separation and enhanced surface area. The versatility and wide range of functionalities offered by metal stannate thin films, especially MTO, make them highly promising for various applications, including gas sensing and photocatalysis. These findings open new possibilities for the development of advanced electronic and energy technologies.

Data availability

The data presented in the current manuscript can be made available upon reasonable request.

Conflicts of interest

There are no conflicts to declare.

Acknowledgements

References

1 Z. Li, H. Yang, L. Zhang, R. Liu and Y. Zhou, Stainless steel mesh-supported three-dimensional hierarchical SnO_2/Zn_2SnO_4 composite for the applications in solar cell, gas sensor, and photocatalysis, *Appl. Surf. Sci.*, 2020, **502**, 144113, DOI: **10.1016/j.apsusc.2019.144113**.

2 V. K. Perla, S. K. Ghosh and K. Mallick, Role of Carbon Nitride on the Resistive Switching Behavior of a Silver Stannate Based Device: An Approach to Design a Logic Gate Using the CMOS-Memristor Hybrid System, *ACS Appl. Electron. Mater.*, 2023, **5**, 1620–1627, DOI: **10.1021/acsaelm.2c01686**.

3 S. Sahoo, A. Sood, R. Kumar, A. Milton, S. M. Choi, Y. J. Jo, I. Hussain and S. S. Han, Rapid in-situ fabrication of $MnSnO_3$ perovskite-based nanocomposites via microwave-assisted approach for supercapacitor devices, *J. Energy Storage*, 2025, **110**, 115368–115378, DOI: **10.1016/j.est.2025.115368**.

4 K. Y. Hwa, A. Santhan, A. Ganguly and T. S. K. Sharma, Point of need simultaneous biosensing of pharmaceutical micropollutants with binder free conjugation of manganese stannate micro-rods on reduced graphene oxide in real-time analysis, *J. Taiwan Inst. Chem. Eng.*, 2022, **131**, 104135–104150, DOI: **10.1016/j.jtice.2021.11.002**.

5 H. R. Barai, M. M. Rahman, M. Adeel and S. W. Joo, $MnSn(OH)_6$ derived $Mn_2SnO_4@Mn_2O_3$ composites as electrode materials for high-performance Supercapacitors, *Mater. Res. Bull.*, 2022, **148**, 111678, DOI: **10.1016/j.materresbull.2021.111678**.

6 Y. K. Duan, Z. W. Li, S. C. Zhang, T. Su, Z. H. Zhang, A. J. Jiao and Z. H. Fu, Stannate-Based Materials as Anodes in Lithium-Ion and Sodium-Ion Batteries: A Review, *Molecules*, 2023, **28**, 28135037, DOI: **10.3390/molecules28135037**.

7 K. Zhou, Y. Zhang, J. Yang, Z. Wang, B. Zhang, Z. Zhou, Y. Zhang, P. Dong and Y. Zhang, Self-templated hydrothermal synthesis of Mn_2SnO_4-$SnO_2@C$ mesoporous nano cube as the anode material for high-performance lithium-ion batteries, *J. Energy Storage*, 2024, **92**, 112001, DOI: **10.1016/j.est.2024.112001**.

8 R. Naeem, M. A. Mansoor, K. Munawar, A. Adnan, T. Zaharinie and M. N. Mohd Zubir, Versatile Fabrication of Binary Composite SnO_2-Mn_2O_3 Thin Films by AACVD for Synergistic Photocatalytic Effect, *J. Electron. Mater.*, 2021, **50**, 3897–3906, DOI: **10.1007/s11664-021-08897-6**.

9 S. Wan, Q. Liu, M. Cheng, Y. Chen and H. Chen, Binary-Metal Mn_2SnO_4 Nanoparticles and Sn Confined in a Cubic Frame with N-Doped Carbon for Enhanced Lithium and Sodium Storage, *ACS Appl. Mater. Interfaces*, 2021, **13**, 38278–38288, DOI: **10.1021/acsami.1c08632**.

10 I. Muneer and M. A. Farrukh, Structural, optical, photoluminescence, photocatalytic and antifungal features of Gd/Mn_2SnO_4 nanocomposite annealed at different

temperatures, *J. Mater. Sci.: Mater. Electron.*, 2022, **33**, 1263–1279, DOI: **10.1007/s10854-021-07420-1**.

11 W. U. Rehman, Y. Xu, X. Sun, I. Ullah, Y. Zhang and L. Li, Bouquet-Like Mn_2SnO_4 Nanocomposite Engineered with Graphene Sheets as an Advanced Lithium-Ion Battery Anode, *ACS Appl. Mater. Interfaces*, 2018, **10**, 17963–17972, DOI: **10.1021/acsami.8b04164**.

12 L. Bigiani, D. Zappa, C. Maccato, A. Gasparotto, C. Sada, E. Comini and D. Barreca, Hydrogen gas sensing performances of p-type Mn_3O_4 nanosystems: The role of built-in Mn_3O_4/Ag and Mn_3O_4/SnO_2 junctions, *Nanomaterials*, 2020, **10**, 15–19, DOI: **10.3390/nano10030511**.

13 B. Gnana Sundara Raj, R. Angulakshmi, N. Baskaran, J. J. Wu, S. Anandan and M. Ashokkumar, Pseudocapacitive performance of $Mn_3O_4–SnO_2$ hybrid nanoparticles synthesized via ultrasonication approach, *J. Appl. Electrochem.*, 2020, **50**, 609–619, DOI: **10.1007/s10800-020-01421-4**.

14 Q. Y. Liu, H. H. Xu, J. Liu, Z. G. Liu, M. X. Huo, X. J. Wang and Y. Sui, Reduced spin damping in inverse spinel Mn_2TiO_4 by ordered occupancy of magnetic ions, *J. Magn. Magn. Mater.*, 2022, **546**, 168864, DOI: **10.1016/j.jmmm.2021.168864**.

15 D. Meena, B. Singh, A. Anand, M. Singh and M. C. Bhatnagar, Phase dependent selectivity shifting behavior of Cd_2SnO_4 nanoparticles based gas sensor towards volatile organic compounds (VOC) at low operating temperature, *J. Alloys Compd.*, 2020, **820**, 153117, DOI: **10.1016/j.jallcom.2019.153117**.

16 M. M. Rahman, M. M. Alam and A. M. Asiri, Fabrication of an acetone sensor based on facile ternary $MnO_2/Gd_2O_3/SnO_2$ nanosheets for environmental safety, *New J. Chem.*, 2017, **41**, 9938–9946, DOI: **10.1039/c7nj01372h**.

17 V. X. Hien, L. H. Phuoc, C. T. Khoa, D. D. Vuong and N. D. Chien, High acetone-sensing performance of bi-phase $α$-/$γ$-Fe_2O_3 submicron flowers grown using an iron plate, *J. Sci.: Adv. Mater. Devices*, 2021, **6**, 27–32, DOI: **10.1016/j.jsamd.2020.09.011**.

18 V. Amiri, H. Roshan, A. Mirzaei, G. Neri and A. I. Ayesh, Nanostructured metal oxide-based acetone gas sensors: A review, *Sensors*, 2020, **20**, 20113096, DOI: **10.3390/s20113096**.

19 D. Lei, J. Xue, Q. Bi, C. Tang and L. Zhang, 3D/2D direct Z-scheme photocatalyst Zn_2SnO_4/CdS for simultaneous removal of Cr(VI) and organic pollutant, *Appl. Surf. Sci.*, 2020, **517**, 146030, DOI: **10.1016/j.apsusc.2020.146030**.

20 A. H. Navidpour and M. Fakhrzad, Photocatalytic activity of Zn_2SnO_4 coating deposited by air plasma spraying, *Appl. Surf. Sci. Adv.*, 2021, **6**, 100153, DOI: **10.1016/j.apsadv.2021.100153**.

21 D. Selvakumaran, A. Manickam, G. Ravi, G. Muthusamy and B. Seshatri, Improved Photocatalytic and Electrochemical Performance of Hydrothermally Synthesized Mg_2SnO_4 Nanocubes and their Effect on Loading with Activated Carbon, *Adv. Mater. Proc.*, 2021, **4**, 109–111, DOI: **10.5185/amp.2019.0004**.

22 L. Munguti and F. Dejene, Effects of Zn: Ti molar ratios on the morphological, optical and photocatalytic properties of $ZnO-TiO_2$ nanocomposites for application in dye removal, *Mater. Sci. Semicond. Process.*, 2021, **128**, 105786, DOI: **10.1016/j.mssp.2021.105786**.

23 K. Palpandi, C. Bhuvaneswari, S. G. Babu and N. Raman, Rational design of ruddlesden-popper phase Mn_2SnO_4 for ultra-sensitive and highly selective detection of chloramphenicol in real-life samples, *New J. Chem.*, 2022, 8729, DOI: **10.1039/d2nj00813k**.

24 K. Y. Hwa, A. Santhan, A. Ganguly and T. S. K. Sharma, Point of need simultaneous biosensing of pharmaceutical micropollutants with binder free conjugation of manganese stannate micro-rods on reduced graphene oxide in real-time analysis, *J. Taiwan Inst. Chem. Eng.*, 2022, **131**, 104135, DOI: **10.1016/j.jtice.2021.11.002**.

25 J. Wang, J. Wang, W. Liu, X. Guo and H. Yang, Sol-gel synthesis of Dictyophora-shaped hierarchically porous Mn_2SnO_4/C materials as anodes for Li-ion batteries, *New J. Chem.*, 2021, **45**, 9538–9549, DOI: **10.1039/d1nj00483b**.

26 Sharanu, A. Kompa, D. Kekuda, K. M. Rao and M. S. Murari, Impact of Cd/Sn molar ratio and annealing temperature on the properties of spin coated Cd_2SnO_4 thin films, *Mater. Chem. Phys.*, 2024, **314**, 128803, DOI: **10.1016/j.matchemphys.2023.128803**.

27 Sharanu, A. Kompa, A. Pal and K. M. Rao, Structural, spectroscopic, and electrical studies of spin-coated ZnO-ZTO thin films for their potential application in photocatalysis and optoelectronics, *Ceram. Int.*, 2023, DOI: **10.1016/j.ceramint.2023.02.199**.

28 Sharanu, A. Kompa, M. S. Murari, D. Kekuda, M. G. Mahesha and K. M. Rao, Effect of cation concentration and annealing temperature on structural, morphological, optical, and electrical properties of spin coated zinc-tin-oxide thin films, *Ceram. Int.*, 2021, **47**, 35294–35301, DOI: **10.1016/j.ceramint.2021.09.072**.

29 B. L. Vijayan, S. G. Krishnan, N. K. M. Zain, M. Harilal, A. Yar, I. I. Misnon, J. O. Dennis, M. M. Yusoff and R. Jose, Large scale synthesis of binary composite nanowires in the Mn_2O_3-SnO_2 system with improved charge storage capabilities, *Chem. Eng. J.*, 2017, **327**, 962–972, DOI: **10.1016/j.cej.2017.06.171**.

30 S. A. Hassanzadeh-Tabrizi, Precise calculation of crystallite size of nanomaterials: A review, *J. Alloys Compd.*, 2023, **968**, 171914, DOI: **10.1016/j.jallcom.2023.171914**.

31 D. H. Manh, T. T. Ngoc Nha, L. T. Hong Phong, P. H. Nam, T. D. Thanh and P. T. Phong, Determination of the crystalline size of hexagonal $La_{1−x}Sr_xMnO_3$ (x = 0.3) nanoparticles from X-ray diffraction - a comparative study, *RSC Adv.*, 2023, **13**, 25007–25017, DOI: **10.1039/d3ra04018f**.

32 J. D. A. Pereira, J. N. Lacerda, I. F. Coelho, C. D. S. C. Nogueira, D. F. Franceschini, E. A. Ponzio, F. B. Mainier and Y. Xing, Tuning the morphology of manganese oxide nanostructures for obtaining both high gravimetric and volumetric capacitance, *Mater. Adv.*, 2020, **1**, 2433–2442, DOI: **10.1039/d0ma00524j**.

33 R. Cestaro, P. Schweizer, L. Philippe, X. Maeder and A. Serrà, Phase and microstructure control of electrodeposited Manganese Oxide with enhanced optical properties, *Appl. Surf. Sci.*, 2022, **580**, 152289, DOI: **10.1016/j.apsusc.2021.152289**.

34 I. Arora, P. Kumar, T. S. Sathiaraj and R. Thangaraj, Structure, optical and electrical properties of sol-gel derived $Zn_{1.5+x}Sn_{1.5-x}O_4$ nanostructured films for optoelectronic applications, *Thin Solid Films*, 2020, **698**, 137871, DOI: **10.1016/j.tsf.2020.137871**.

35 S. Ren, T. Tang, Y. Liu, C. Li, L. Wu, W. Li, J. Zhang, W. Wang and L. Feng, Annealing atmosphere effects on the surface properties of Cd_2SnO_4 thin films obtained by RF sputtering, *Mater. Sci. Semicond. Process.*, 2018, **75**, 269–275, DOI: **10.1016/j.mssp.2017.11.017**.

36 W. ur Rehman, Z. Jiang, Z. Qu, Y. Xu, X. Wang and I. Ullah, Preparation of Mn_2SnO_4 wrapped with N-doped reduced graphene oxide as a stable anode material for lithium–ion storage, *J. Alloys Compd.*, 2023, **939**, 168829, DOI: **10.1016/j.jallcom.2023.168829**.

37 H. R. Barai, M. M. Rahman, M. Adeel and S. W. Joo, MnSn(OH)6 derived $Mn_2SnO_4@Mn_2O_3$ composites as electrode materials for high-performance Supercapacitors, *Mater. Res. Bull.*, 2022, **148**, 111678, DOI: **10.1016/j.materresbull.2021.111678**.

38 A. Kocyigit, Structural, optical and electrical characterization of Mn_3O_4 thin films via Au composite, *Mater. Res. Express*, 2018, **5**, 066422, DOI: **10.1088/2053-1591/aacb0d**.

39 M. Borrega, S. Päärnilä, L. G. Greca, A. S. Jääskeläinen, T. Ohra-Aho, O. J. Rojas and T. Tamminen, Morphological and wettability properties of thin coating films produced from technical lignins, *Langmuir*, 2020, **36**, 9675–9684, DOI: **10.1021/acs.langmuir.0c00826**.

40 R. Dridi, C. Mrabet, A. Labidi, N. Mahdhi, A. Amlouk and M. Amlouk, Electrical conductivity of Zn_2SnO_4 thin films along with wettability and EtOH-sensing, *J. Alloys Compd.*, 2017, **708**, 769–779, DOI: **10.1016/j.jallcom.2017.03.055**.

41 C. Mrabet, R. Dridi, N. Mahdhi and M. Amlouk, Mechanism of wettability conversion on sprayed Zn_2SnO_4 thin films surfaces modified by thermal annealing in air, *J. Alloys Compd.*, 2017, **725**, 765–772, DOI: **10.1016/j.jallcom.2017.07.212**.

42 Sharanu, A. Kompa, D. Kekuda and K. M. Rao, A way to sense H2S gas using nanostructured Zinc-Stannate (Zn_2SnO_4) ternary oxide, *Microchem. J.*, 2025, **210**, 112989, DOI: **10.1016/j.microc.2025.112989**.

43 P. Wang, S. Z. Wang, Q. Han, D. Q. Zou, W. K. Zhao, X. D. Wang, C. Luo, X. Yang, X. Wu and W. F. Xie, Construction of Hierarchical α-Fe_2O_3/SnO_2 Nanoball Arrays with Superior Acetone Sensing Performance, *Adv. Mater. Interfaces*, 2021, **8**, DOI: **10.1002/admi.202001831**.

44 J. Zhang, X. Jia, T. Liu, J. Yang, S. Wang, Y. Li, D. Shao, L. Feng and H. Song, Facile strategy to synthesize porous GO/ZnO heterostructure for enhanced acetone gas sensing properties, *Sens. Actuators, B*, 2022, **359**, 131601, DOI: **10.1016/j.snb.2022.131601**.

45 X. Yao, B. Zhang, S. Cui, S. Yang and X. Tang, Fabrication of $SnSO_4$-modified TiO_2 for enhance degradation performance of methyl orange (MO) and antibacterial activity, *Appl. Surf. Sci.*, 2021, **551**, 149419, DOI: **10.1016/j.apsusc.2021.149419**.

46 A. Boughelout, R. Macaluso, M. Kechouane and M. Trari, Photocatalysis of rhodamine B and methyl orange degradation under solar light on ZnO and Cu2O thin films, *React. Kinet., Mech. Catal.*, 2020, **129**, 1115–1130, DOI: **10.1007/s11144-020-01741-8**.